

Perfect sound absorption of Helmholtz resonators with embedded channels in petal shape

Cite as: J. Appl. Phys. **130**, 135102 (2021); <https://doi.org/10.1063/5.0064811>

Submitted: 27 July 2021 • Accepted: 13 September 2021 • Published Online: 01 October 2021

Mingyu Duan, Chenlei Yu, Wei He, et al.



View Online



Export Citation



CrossMark

ARTICLES YOU MAY BE INTERESTED IN

[Influence of oxygen adsorption from atmosphere on surface tension of liquid silicon](#)
Journal of Applied Physics **130**, 135101 (2021); <https://doi.org/10.1063/5.0062062>

[Realizing high thermoelectric performance in N-type Bi₂Te₃ compounds by Sb nano-precipitates](#)

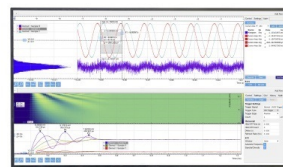
Journal of Applied Physics **130**, 135103 (2021); <https://doi.org/10.1063/5.0066932>

[The correlation between the covalent bonds and magnetocaloric properties of the Mn_{2-x}Fe_xP_yGe_{1-y}M_z compounds](#)

Journal of Applied Physics **130**, 133901 (2021); <https://doi.org/10.1063/5.0056190>

Challenge us.

What are your needs for periodic signal detection?



Zurich
Instruments



Perfect sound absorption of Helmholtz resonators with embedded channels in petal shape

Cite as: J. Appl. Phys. **130**, 135102 (2021); doi: [10.1063/5.0064811](https://doi.org/10.1063/5.0064811)

Submitted: 27 July 2021 · Accepted: 13 September 2021 ·

Published Online: 1 October 2021



Mingyu Duan,^{1,2} Chenlei Yu,^{1,2} Wei He,^{1,2} Fengxian Xin,^{1,2,a)}  and Tian Jian Lu^{2,3,4,b)}

AFFILIATIONS

¹State Key Laboratory for Strength and Vibration of Mechanical Structures, Xi'an Jiaotong University, Xi'an 710049, People's Republic of China

²MOE Key Laboratory for Multifunctional Materials and Structures, Xi'an Jiaotong University, Xi'an 710049, People's Republic of China

³State Key Laboratory of Mechanics and Control of Mechanical Structures, Nanjing University of Aeronautics and Astronautics, Nanjing 210016, People's Republic of China

⁴MIIT Key Laboratory of Multi-functional Lightweight Materials and Structures (MLMS), Nanjing University of Aeronautics and Astronautics, Nanjing 210016, People's Republic of China

^{a)}Author to whom correspondence should be addressed: fengxian.xin@gmail.com

^{b)}Electronic mail: tjlu@nuaa.edu.cn

ABSTRACT

The acoustic metamaterial in the form of a petal-shaped channel embedded Helmholtz resonator (P-CEHR) is proposed for perfect sound absorption. According to theoretical predictions, numerical simulations, and experiments, the P-CEHR achieves perfect low-frequency (e.g., 200 Hz) sound absorption across a deep subwavelength thickness (e.g., 1/34 of the corresponding acoustic wavelength). Compared with the circular-shaped channel embedded Helmholtz resonator, the sound absorption peak and bandwidth of P-CEHR are significantly improved (e.g., increased by 20.9% and 60.0%, respectively) under fixed overall dimensions. Physically, the introduction of the petal shape changes the fluid dynamic characteristics of the channel, resulting in the periodic distribution of particle velocity along the circumferential direction and the expansion of the area of the viscous boundary layer. By adjusting the morphology of the embedded channel, the tortuosity ratio and the relative static flow resistance of the channel can be regulated appropriately, so that the resonator can meet the acoustic impedance matching condition and achieve excellent sound absorption performance. This work provides a method for improving the performance of acoustic absorption metamaterials with built-in air channels and has guiding significance for the control of low-frequency noise.

Published under an exclusive license by AIP Publishing. <https://doi.org/10.1063/5.0064811>

I. INTRODUCTION

As two traditional sound absorbers, porous materials^{1–3} and micro-perforated panels^{4–6} have been widely used in engineering noise reduction. However, due to the long wavelength of the low-frequency sound waves, these traditional sound absorbers cannot achieve satisfactory sound absorption performance at a small thickness below 1000 Hz. The emergence of acoustic metamaterials^{7–13} tries to solve this problem. By using the loss in acoustic metamaterials appropriately,¹⁴ sound insulation,^{15,16} sound wave manipulation,^{17–19} and also sound energy absorption^{20,21} can be realized. With the design of coiled space,^{22–26} multilayer resonators,^{27–29} or embedded channels,^{30–34} perfect sound absorption

can be achieved at hundreds of hertz by acoustic metamaterials with deep subwavelength thickness. However, the realization of perfect sound absorption requires the acoustic metamaterials to meet the acoustic impedance matching condition; that is, at the same frequency, the acoustic resistance and acoustic reactance must be equal to 1 and 0, respectively.³² Also, the impedance matching condition affects the reflection and transmission performance of acoustic metamaterials. Therefore, acoustic impedance regulation has become the key problem to improve the acoustic performance of metamaterials.

In order to solve this problem, some novel design strategies to reduce the acoustic impedance mismatch of metamaterials have been proposed using tapered labyrinthine structures,^{35,36} acoustic

passive phased array,³⁷ helical structure,³⁸ and impedance matching layers.³⁹ Here, starting from another path, we achieve acoustic impedance regulation and sound absorption performance improvement of acoustic metamaterials through the cross-sectional shape design of the embedded channel. Our previous works on the fluid theory of rough channels^{40–42} show that the axial roughness and circumferential roughness (i.e., petal roughness) of the channel will affect its hydrodynamic performance, resulting in the deformation of the flow field in the channel and the periodic concentration effect of flow velocity. The follow-up works on this basis show that considering the roughness effect in micro-perforated panels^{43,44} and porous materials,^{45,46} higher acoustic resistance and better sound absorption performance can be achieved.

Inspired by the above contents, we try to apply the roughness effect to the design of acoustic metamaterials in order to find new ways to adjust the acoustic impedance and improve the performance of acoustic metamaterials. In this work, the channel embedded Helmholtz resonator (CEHR) is selected as an example of acoustic metamaterials to illustrate such a performance improvement method. Based on the fluid theory of rough channels, the petal-shaped channel embedded Helmholtz resonator (P-CEHR) is obtained by replacing the channel of the previous proposed circular-shaped channel embedded Helmholtz resonator (C-CEHR) by a petal-shaped channel. Theoretical predictions, numerical simulations, and experimental tests show that P-CEHR has good sound absorption and wide absorption bandwidth, which are better than the traditional C-CEHR. Moreover, the mechanism for this performance improvement is analyzed through impedance analysis, complex frequency plane analysis, finite element (FE) simulation, and fluid dynamic parameters discussion.

II. THEORETICAL MODEL

According to Figs. 1(a) and 1(b), the CEHRs are composed of a straight embedded channel and an air cavity. Plane sound waves are considered to normally incident on the upper side of the CEHRs. Acoustically, the 3D-printed walls of the channels and cavities made of photosensitive resin (with density of 1300 kg/m^3 , Young's modulus of 2370 MPa , and Poisson's ratio of 0.41) can be considered as rigid in theoretical and numerical modeling. Under the excitation of the sound waves with a specific resonant frequency, Helmholtz resonance occurs in CEHR. The air in the channel and the air in the cavity will perform as an oscillator and a spring of the resonant system, respectively. Due to the viscosity of air, the oscillation of the air column in the channel will cause friction between air and the wall of the channel, resulting in energy dissipation and sound absorption. For the traditional C-CEHR, its embedded channel is a simple circular pipe, as shown in Fig. 1(a). While in order to improve the sound absorption performance of the CEHR, the embedded channel of P-CEHR is designed as petal shape to regulate its fluid dynamic performance and acoustic impedance, as shown in Figs. 1(b) and 1(c). Referring to Fig. 1(c), in order to facilitate the acoustic modeling of the petal-shaped channel through the fluid theory of rough channels,⁴¹ the form of cross-sectional boundary in the channel is described as a closed curve with a sinusoidal perturbation in the polar coordinate system, which can be written as follows:

$$\rho = d[0.5 - \varepsilon \sin(n\theta)], \quad (1)$$

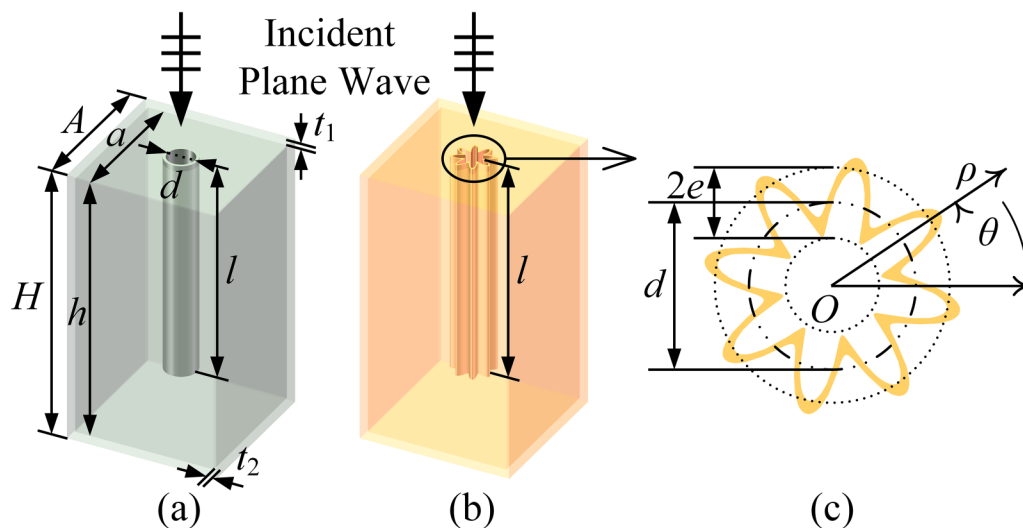


FIG. 1. (a) Geometry of the C-CEHR with channel diameter $d = 10 \text{ mm}$, channel length $l = 40 \text{ mm}$, cavity side length $a = 25.6 \text{ mm}$, cavity depth $h = 48 \text{ mm}$, facesheet thickness $t_1 = 2 \text{ mm}$, wall thickness $t_2 = 1 \text{ mm}$, total side length $A = 27.6 \text{ mm}$, and total thickness $H = 50 \text{ mm}$. (b) Geometry of the P-CEHR with the same channel length $l = 40 \text{ mm}$ and the same facesheet perforation ratio $\phi = S_n/S_a = 0.03$ as the C-CEHR, where S_n is the inner cross-sectional area of the channel and S_a is the inner cross-sectional area of the cavity. (c) Cross section of the petal-shaped channel in the polar coordinate system with channel average diameter $d = 5 \text{ mm}$, channel diameter perturbation amplitude $e = 1 \text{ mm}$, and petal shape wavenumber $n = 8$. It should be noted that the selection of all the above dimensions is only an example of the designed metamaterial, which does not mean that the metamaterial is limited to the above dimensions.

where ρ and θ are separately the polar radius and polar angle and $\varepsilon = e/d$ and n are defined as the relative roughness and wavenumber of the channel to describe the radial relative amplitude and circumferential distribution density of the petal shape, respectively. Let ε be equal to 0, Eq. (1) can be reduced to the circular channel boundary.

In order to predict the sound absorption coefficient of CEHRs more accurately, the theoretical modeling process in this work is similar to the sound absorption theory of the micro-perforated panel proposed by Maa,⁵ instead of the spring-mass oscillator analog model of the Helmholtz resonator. Therefore, it is necessary to calculate the acoustic impedance of the channel and cavity, respectively. According to the model of Johnson *et al.*⁴⁷ and Pride *et al.*,⁴⁸ the acoustic impedance of an arbitrary shaped channel can be calculated by

$$Z_n = j\omega\rho_0 l \left\{ \frac{v_0}{j\omega q_0} \left\{ 1 - \chi + \chi \sqrt{1 + \left(\frac{8\alpha_\infty q_0}{3\Lambda} \right)^2 \frac{j\omega}{v_0}} \right\} + \alpha_\infty \right\}, \quad (2)$$

where j is the imaginary unit, ω is the angular frequency, $\rho_0 = 1.29 \text{ kg/m}^3$ is the density of air, $v_0 = \mu_0/\rho_0$ and $\mu_0 = 1.81 \times 10^{-5} \text{ Pa s}$ are separately the kinematic viscosity and dynamic viscosity of air, $\Lambda = \sqrt{8\mu_0\alpha_\infty/\sigma}$ is the viscous characteristic length, $q_0 = \mu_0/\sigma$ is the viscous permeability, σ is the static flow resistivity, and α_∞ is the tortuosity. As for the straight channels with a constant cross section along the fluid flow direction, α_∞ should be equal to 1. The tortuosity ratio $\chi = \frac{\alpha_\infty}{4(\alpha_0 - \alpha_\infty)}$ is a dimensionless parameter introduced by Pride to adjust the low-frequency limit of Eq. (2), where α_0 is the static tortuosity. For the calculation of Eq. (2), there are still two key fluid dynamic parameters to be solved, which rely on the flow field in the channel, namely, static flow resistivity σ and static tortuosity α_0 . Based on the fluid theory of rough channels,⁴¹ the cross-sectional velocity field of the fully developed Stokes flow in a petal-shaped channel has been solved in the polar coordinate system as follows:

$$u = \{2 - 2(1 - 2\varepsilon)^{-2} + [8(1 - 2\varepsilon)^{-4} - 8]\rho^2\} \left(\frac{2e^{-\frac{n}{12.5}}}{1 + e^{-\frac{n}{12.5}}} - 1 \right) - 2^{n+2}\varepsilon\rho^n \sin(n\theta) + 2 - 8\rho^2. \quad (3)$$

When $\varepsilon = 0$ or $n = 0$, Eq. (3) reduces to the velocity field of a circular-shaped channel, as $u = 2 - 8\rho^2$. Accordingly, the relative static flow resistivity of the petal-shaped channel has also been solved via the fluid theory of rough channels⁴¹ to characterize the influence of the channel shape on the flow field as

$$\frac{\sigma_p}{\sigma_c} = \frac{1}{(1 - 2\varepsilon)^4} + \left(1 - \frac{1}{(1 - 2\varepsilon)^4} \right) \frac{2e^{-\frac{1}{12.5}n}}{1 + e^{-\frac{1}{12.5}n}}, \quad (4)$$

where $\sigma_c = 32\mu_0/d^2$ is the static flow resistivity of the circular-shaped channel. Hence, the static flow resistivity of the petal-shaped channel σ_p can be obtained by Eq. (4). Additionally, the

static tortuosity α_0 is defined as⁴¹

$$\alpha_0 = \langle u_m^2(M) \rangle_V / u^2(M_0), \quad (5)$$

where $u_m(M)$ is the microscopic flow velocity at the position M in the channel and $u(M_0)$ is the macroscopic flow velocity of the representative unit M_0 in the channel obtained by the volume average of the microscopic velocity $u_m(M)$ in the representative unit with volume V , i.e., $u(M_0) = \langle u(M) \rangle_V$. With the use of the flow velocity field represented in Eq. (3), α_0 can be solved under different petal shape parameters. Substituting Eqs. (4) and (5) into Eq. (2), the acoustic impedance of the petal-shaped channel can be finally calculated. Let $\varepsilon = 0$ or $n = 0$, Eq. (2) can be reduced to the acoustic impedance of a traditional circular-shaped channel. Considering the end effect caused by the cross section mutations at the inlet and outlet of the channel, Eq. (2) should be modified as⁵

$$Z'_n = Z_n + \frac{4\sqrt{2}\mu_0 y}{d} + 0.85dj\omega\rho_0, \quad (6)$$

where $y = d\sqrt{\rho_0\omega/4\mu}$ is a dimensionless parameter representing the ratio of channel diameter to the viscous boundary layer thickness.

According to the impedance transfer method, the acoustic impedance of the air cavity can be written as⁴⁹

$$Z_c = -jZ_0 \cot(k_0\delta_1 h), \quad (7)$$

where $Z_0 = \rho_0 c_0$ is the characteristic acoustic impedance of air and $c_0 = 343 \text{ m/s}$ and $k_0 = \omega/c_0$ are separately the sound speed and wavenumber of air, respectively. The cavity depth correction factor $\delta_1 = (V_c - V_n)/V_c$ is introduced here to exclude the cavity volume occupied by the embedded channel, in which V_n and V_c are the volumes of the channel and the air cavity, respectively.

Then, the surface acoustic impedance ratios of the CEHRs can be calculated as

$$Z_s = \delta_2(Z'_n/\phi + Z_c)/Z_0, \quad (8)$$

where $\delta_2 = A^2/a^2$ is the correction factor to consider the effect of the cavity wall thickness on the total surface acoustic impedance. As for the sound absorbers with rigid backing under the normal incidence of plane sound waves, the sound absorption coefficients of CEHRs can be calculated as⁴⁹

$$\alpha = 1 - |R|^2 = \frac{4\text{Re}(Z_s)}{[1 + \text{Re}(Z_s)]^2 + [\text{Im}(Z_s)]^2}, \quad (9)$$

where $R = (Z_s - 1)/(Z_s + 1)$ is the reflection coefficient and $\text{Re}(Z_s)$ and $\text{Im}(Z_s)$ are the real part and imaginary part of the surface acoustic impedance ratios, i.e., the surface acoustic resistance ratios and surface acoustic reactance ratios of CEHRs, respectively.

III. FINITE ELEMENT MODEL

The numerical simulations of the acoustic performance of the CEHRs are based on COMSOL Multiphysics software.⁵⁰ In order

to show the internal meshes, we selected 3/4 of the complete finite element (FE) model for display, as shown in Fig. 2. The three-dimensional (3D) FE model of CEHR is established and 3D numerical calculation is carried out. Due to the strong impedance mismatch between CEHR wall and air, all solid parts of CEHR are simplified to acoustic rigidity in order to improve the calculation efficiency. Therefore, we only need to establish the FE model of air domain. The geometry of CEHR is established parametrically. When we adjust the relative roughness of the channel shape from 0 to 0.2, the geometry of the FE model can be converted from C-CEHR to P-CEHR. The green part at the top of the FE model shown in Fig. 2 is the pressure acoustics field. The upper boundary of the pressure acoustics field is set as the plane wave incident condition to simulate the sound wave excitation vertically incident on the CEHR from the semi-infinite air domain, and the sound pressure amplitude is 1 Pa. In order to simulate the periodicity of CEHRs, the front and back sides and the left and right sides of the pressure acoustic field are set as two pairs of periodic boundary conditions, respectively. The orange part of the FE model is the thermoviscous acoustics field, as shown in Fig. 2. In this sound field, the energy loss caused by the viscosity of the air in CEHR can be calculated. The boundaries connected to the inner walls of CEHR are the default acoustic hard boundaries. In order to describe the continuity condition between the pressure acoustic field and the thermoviscous acoustic field, the interface between the two sound fields is set as the pressure–thermoviscous interaction boundary.

To ensure the calculation accuracy, the mesh quality of the channel needs to be refined. First, the upper surface of the

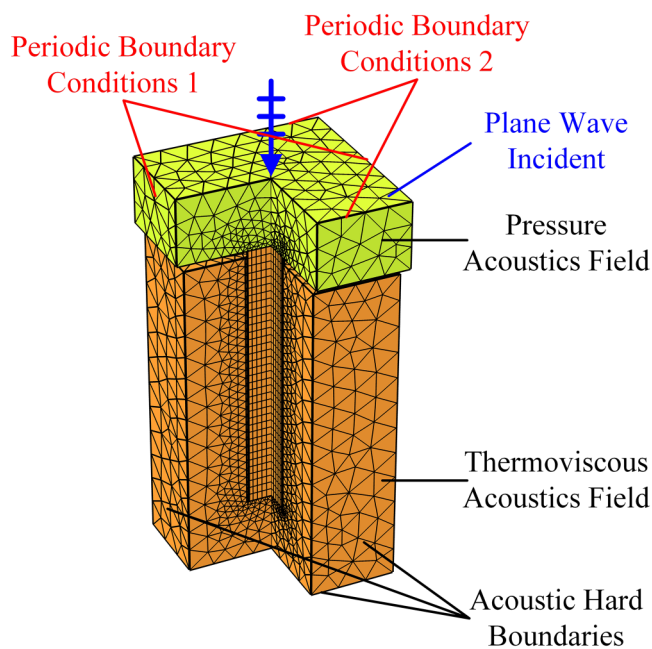


FIG. 2. A three-dimensional finite element (FE) model of CEHR.

petal-shaped channel is divided into free triangle meshes. On this basis, the triangular prism mesh of the channel is obtained by sweeping the triangular meshes along the axis of the channel. The rest of the FE model is divided by free tetrahedral meshes. The distributions of particle vibration velocity, sound pressure, and energy loss density inside and on the CEHR can be obtained by frequency domain research. Finally, the surface acoustic impedance ratio and sound absorption coefficient of the CEHR can be calculated by the average sound pressure and the average particle vibration velocity of the upper surface of CEHR. Using the 2D plot group in COMSOL, the physical field of the cross section of the channel can be drawn in the 2D contour map to facilitate the subsequent mechanism analysis.

IV. RESULTS AND DISCUSSION

In order to verify the theoretical predictions and numerical simulations, the C-CEHR and P-CEHR samples are fabricated by stereolithographic (SLA) 3D-printing using photosensitive resin (with density of 1300 kg/m^3 , Young's modulus of 2370 MPa, and Poisson's ratio of 0.41), as shown in Figs. 3(a)–3(d). The experimental tests are carried out via Brüel & Kjær 4206 impedance tube testing system according to the ASTM standard test method⁵¹ for the impedance and absorption of acoustical materials using a tube, two microphones, and a digital frequency analysis system, as shown in Fig. 3(e). The inner diameter of the Brüel & Kjær 4206 impedance tube used in the experimental tests is 100 mm, which is equivalent to the outer diameter of the 3D-printed samples in Figs. 3(c) and 3(d). In this setting, the measurement frequency range of the impedance tube is from 50 to 1600 Hz. In order to ensure the measurement accuracy at low frequencies, the distance between the two microphones is set to a wide spacing, i.e., a distance of 100 mm.⁵²

The sound absorption coefficients of the C-CEHR and P-CEHR are shown in Fig. 4(a). It can be seen that the results of the theoretical predictions, numerical simulations, and experimental tests are in good agreements. The P-CEHR reaches perfect sound absorption (i.e., $\alpha \geq 0.99$) at 200 Hz and has a half-absorption bandwidth ($\alpha \geq 0.5$) of 56 Hz. It is worth noticing that the total thickness of the P-CEHR is only 50 mm, which means that perfect sound absorption is achieved through a deep subwavelength scale as $1/34$ of the corresponding acoustic wavelength. From this perspective, the P-CEHR can be classified as a new acoustic metamaterial with compact structure and excellent sound absorption performance. In sharp contrast, the C-CEHR only has an absorption peak value of 0.82 at 204 Hz and a half-absorption bandwidth of 34 Hz. With the overall size unchanged, by introducing petal shape, the absorption peak and half-absorption bandwidth of the CEHR are increased by 20.9% and 60.0%, respectively.

The sound absorption improvement of the CEHR can be explained by the regulation effect of the channel shape on the acoustic impedance of the CEHR. It can be known from Eq. (9) that the realization of perfect sound absorption requires the sound absorber to strictly satisfy the acoustic impedance matching condition, i.e., $\text{Re}(Z_s) = 1$ and $\text{Im}(Z_s) = 0$ are realized simultaneously. Since the absolute value of $\text{Im}(Z_s)$ is much larger than that of $\text{Re}(Z_s)$ at low frequencies, the peak frequency of the sound absorption coefficient is generally determined by the zero point of $\text{Im}(Z_s)$

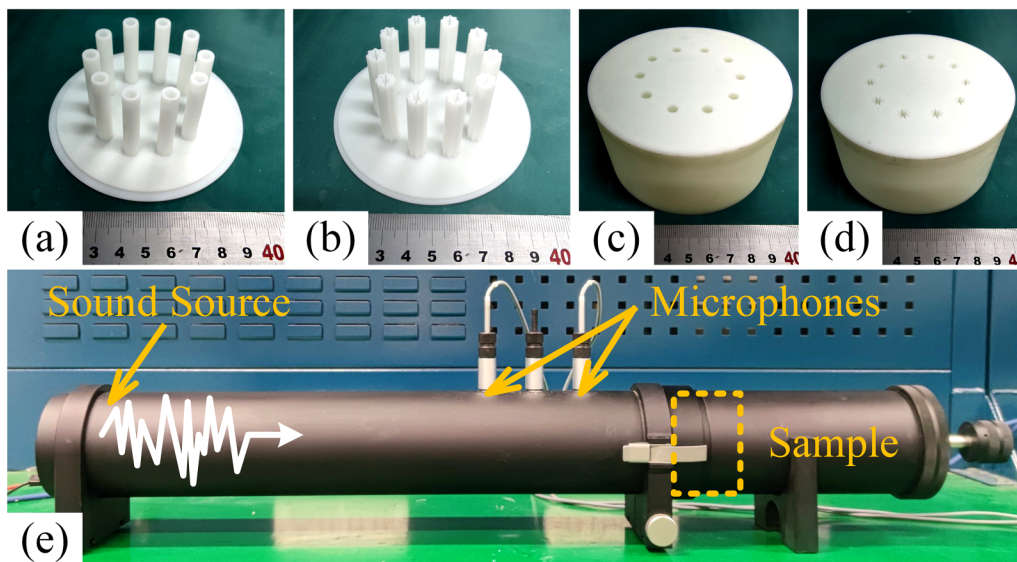


FIG. 3. (a) and (b) 3D-printed perforated facesheets with circular- and petal-shaped embedded channels, which have the same perforation ratio as $\phi = 0.03$. (c) and (d) 3D-printed C-CEHR and P-CEHR samples constructed by bonding the facesheets and cavities. (e) Experimental setup of the standard Brüel & Kjaer 4206 impedance tube testing system.

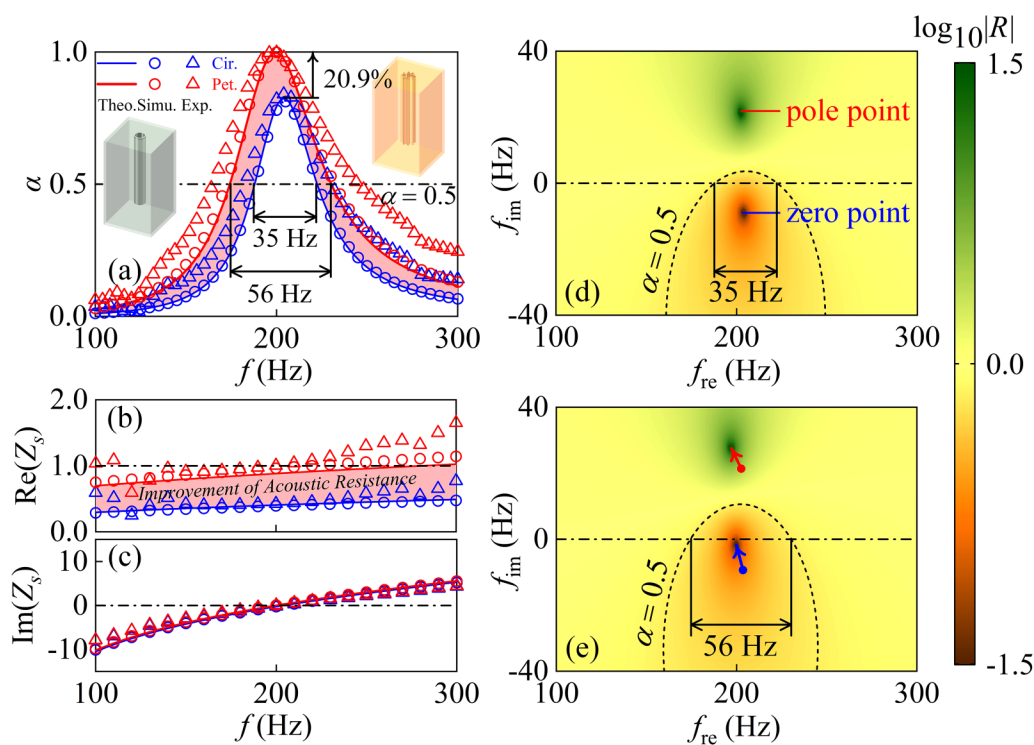


FIG. 4. Acoustic performance comparison between the C-CEHR and P-CEHR: (a) Sound absorption coefficients, (b) surface acoustic resistance ratios, and (c) surface acoustic reactance ratios of the C-CEHR and P-CEHR. The blue curves/circles/triangles and red curves/circles/triangles indicate the theoretical/numerical/experimental data of the C-CEHR and P-CEHR, respectively. (d) and (e) Complex frequency plane expressions for the reflection coefficients of the C-CEHR and P-CEHR.

while the peak value is related to $\text{Re}(Z_s)$. As shown in Fig. 4(c), the acoustic reactance of the C-CEHR and P-CEHR are identical in the frequency range of interest, which both reach the zero at 200 Hz. Therefore, the absorption peaks of the C-CEHR and P-CEHR appear almost at the same frequency. Meanwhile, according to Fig. 4(b), the acoustic resistance of the CEHR shows a significant improvement after introducing the petal-shaped channel. Compared with the C-CEHR, $\text{Re}(Z_s)$ of the P-CEHR is much closer to 1 near the peak frequency, which makes the P-CEHR reach the acoustic impedance matching condition for perfect sound absorption and have higher absorption peak and wider half-absorption bandwidth. It can be seen that the regulation of the channel shape to the acoustic impedance has a positive effect on the sound absorption performance of CEHR.

The damping state of the CEHRs at resonant frequency is discussed via a complex frequency plane analysis, as shown in Figs. 4(d) and 4(e). By extending the frequency f in the theoretical model to the complex domain as $f' = f_{re} + jf_{im}$, the reflection coefficient R of the CEHR can be expressed as a function of real frequency f_{re} and imaginary frequency f_{im} and plotted in the complex frequency plane. For a hypothetical lossless resonant system, the zero point and the pole-point of the reflection coefficient will be conjugate symmetric about the real frequency axis (i.e., $f_{im} = 0$) in the complex frequency plane. For the actual lossy system, the position of the zero-pole pair will change due to the introduction of loss. With the increase in the loss, part of the energy leakage will be balanced and the zero point will shift to the real frequency axis. When the energy leakage of the system is completely balanced by the energy loss, the zero point will fall on the real frequency axis, which means that the critical damping state and completely energy absorption (i.e., $R = 0$ and $\alpha = 1$) will be realized in the real frequency domain. As for the C-CEHR, it can be seen from Fig. 4(d) that its zero-point falls below the real frequency axis. This means that the C-CEHR is in the under damping state, so that it performs imperfect sound absorption performance. By introducing the petal-shaped channel, the zero-pole pair of the P-CEHR shifts upward in the direction of the arrows, as shown in Fig. 4(e). It can be seen that the zero point of the P-CEHR finally falls on the real frequency axis, which leads to the critically damping state and perfect sound absorption. Besides, the shift of the zero point also increases the half-absorption bandwidth of the P-CEHR. In short, due to the introduction of the petal-shaped channel, the damping state of the CEHR is transited from the under damping state to critically damping state, so that the P-CEHR shows advantages in the sound absorption peak and bandwidth.

In order to explain the physical mechanism of the acoustic impedance regulation and damping state transition of the CEHR, the particle vibration velocity and energy dissipation density in the embedded channels at 200 Hz are plotted in Fig. 5 according to numerical simulations. As shown in Fig. 5(a), for the circular-shaped channel, the velocity field in most areas far away from its boundary is basically uniform, while the annular velocity gradient can be clearly observed near its boundary. This annular area with velocity gradient is the viscous boundary layer of the channel, in which the particle vibration velocity increases sharply from 0 to that at the center of the channel. For the petal-shaped channel, due to the change in the channel boundary shape, the particle vibration

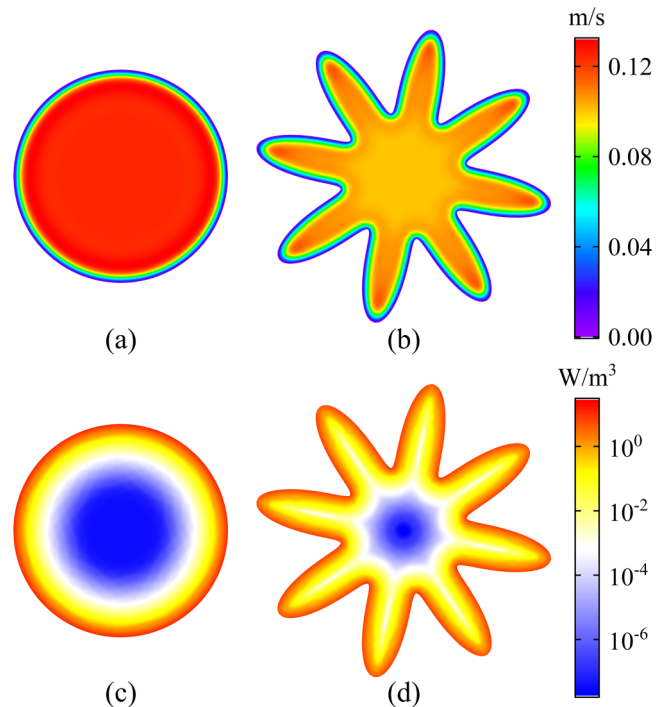


FIG. 5. (a) and (b) Particle vibration velocity distribution on the cross section of circular and petal-shaped channels at 200 Hz. (c) and (d) Energy dissipation density distribution on the cross section of circular and petal-shaped channels at 200 Hz.

velocity field becomes petal-shaped, and the particle velocity is periodically distributed along the circumferential direction, as shown in Fig. 5(b). The viscous boundary layer of the petal-shaped channel is still generated near the channel boundary, with a shape change from annular to petal-shape. In this way, the area of the viscous boundary layer is expanded. From the perspective of viscous dissipation, the larger velocity gradient in the viscous boundary layer of the channel will lead to greater energy dissipation. Therefore, according to Fig. 5(c), the energy dissipation of the circular-shaped channel mainly occurs in the viscous boundary layer, which is on the order of 10^0 W/m^3 . However, since the velocity gradient in the area far from the boundary is almost non-existent, the energy dissipation in most areas of the channel center tends to zero. While in the petal-shaped channel, as shown in Fig. 5(d), the maximum energy dissipation also occurs at the viscous boundary layer with the order of 10^0 W/m^3 . And the energy dissipation in each piece of the petal remains at a relative high value above the order of 10^{-2} W/m^3 . Overall, the total energy dissipation in the petal-shaped channel is higher than that in the circular-shaped channel. It can be concluded that the introduction of the petal shape changes the fluid dynamic performance of the channel and expands the area of the viscous boundary layer in the channel, resulting in more energy dissipation at the peak frequency. In fact, the increase in the energy dissipation means the increase in the acoustic resistance. Therefore, the surface acoustic resistance

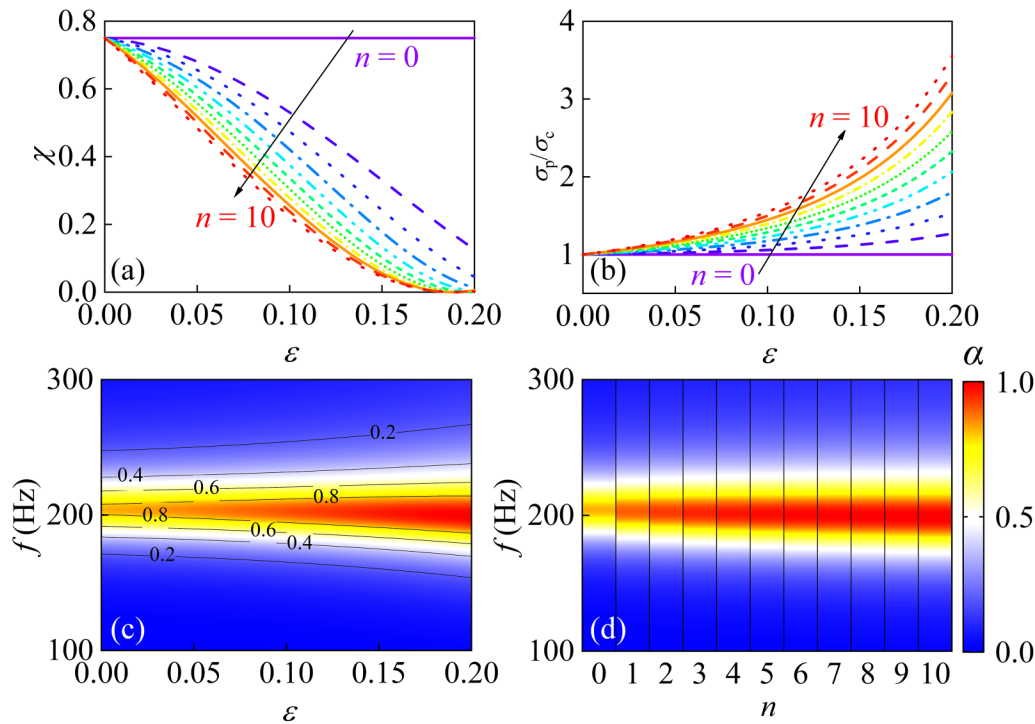


FIG. 6. Effects of roughness on fluid dynamic parameters and sound absorption performance of the CEHR: (a) and (b) Effects of the relative roughness and wavenumber on the tortuosity ratio and the relative static flow resistance of the channel. (c) and (d) Effects of the relative roughness and wavenumber on sound absorption coefficient of the CEHR. When the relative roughness or wavenumber is changed, other geometric parameters of the CEHR are fixed. Due to geometric constraints, the wavenumber can only be a natural number.

ratio of P-CEHR increases to 1 at 200 Hz, so as to reach the acoustic impedance matching condition for perfect sound absorption, as shown in Fig. 4(b).

In order to explain how the relative roughness ε and wavenumber n of the channel can tailor the sound absorption performance of the CEHR by regulating the fluid dynamic parameters, the relationship between the morphology of the petal shape and the fluid dynamic performance of the channel is quantitatively characterized in Figs. 6(a) and 6(b). Figure 6(a) shows the effect of the relative roughness and wavenumber on the tortuosity ratio χ of the channel. With the increase in relative roughness or wavenumber, the fluid velocity field in the channel changes from the circular shape to the petal shape. This causes a more unevenly distribution of the velocity field in the channel, which leads to a larger static tortuosity α_0 according to Eq. (5). In turn, it can be seen in Fig. 6(a) that the tortuosity ratio is reduced with the increase in relative roughness or wavenumber. The influence of the relative roughness and wavenumber on the relative static flow resistance σ_p/σ_c of the channel is shown in Fig. 6(b). The increase in the relative roughness or wavenumber leads to the expansion of the viscous boundary layer area, which increases the static flow resistance of the channel. As a result, when the relative roughness or wavenumber is increased, the relative static flow resistance of the channel increases, as shown in Fig. 6(b). In this way, by elaborately

adjusting the morphology of the petal shape (i.e., the relative roughness ε and wavenumber n), the fluid dynamic performance and the acoustic impedance of the embedded channel can be regulated according to Eqs. (2)–(5), so as to customize the sound absorption performance of the CEHR.

The relationship between channel morphology and CEHR sound absorption performance is further plotted in two sound absorption spectra, as shown in Figs. 6(c) and 6(d). The channel morphology is described by two geometric parameters, i.e., the relative roughness and the roughness wavenumber. As shown in Figs. 6(c) and 6(d), with the increase in the relative roughness or the roughness wavenumber, the sound absorption peak increases and the sound absorption bandwidth enlarges. As the relative roughness increases from 0 to 0.2 or the wavenumber increases from 0 to 10, the sound absorption peak value gradually increases from a relatively low level (about 0.83) to complete sound absorption (above 0.99). In fact, the peak frequency of the CEHR also decreased slightly, but this effect is not significant. The results show that the sound absorption performance of the CEHR can be improved by adjusting the relative roughness and the roughness wavenumber of the channel. This work provides a method for acoustic impedance regulation and sound absorption performance improvement of acoustic metamaterials with built-in air channels and has guiding significance for the control of low-frequency noise.

V. CONCLUSIONS

In this work, we propose a method to improve the sound absorption performance of the acoustic metamaterials without changing their overall size. On this basis, a new acoustic metamaterial with deep subwavelength thickness, namely, the petal-shaped channel embedded Helmholtz resonator, is designed for perfect sound absorption. By tailoring the cross-sectional shape of the embedded channel, the area of the viscous boundary layer of the channel is expanded, so as to change the fluid dynamic performance and acoustic resistance of the channel. As a result, the acoustic impedance of the Helmholtz resonator is regulated to satisfy the impedance matching condition for perfect sound absorption. This work contributes to the novel structural design and performance improvement of acoustic metamaterials.

ACKNOWLEDGMENTS

This work was supported by the National Natural Science Foundation of China (NNSFC) (Nos. 52075416, 11772248, and 11761131003), the Fundamental Research Funds for the Central Universities, and the Open Fund of the State Key Laboratory of Mechanics and Control of Mechanical Structures (Nos. MCMS-I-0219K01 and MCMS-E-0219K02). The authors declare that they have no known competing financial interests or personal relationships that could have appeared to influence the work reported in this article.

DATA AVAILABILITY

The data that support the findings of this study are available from the corresponding author upon reasonable request.

REFERENCES

- ¹T. J. Lu, A. Hess, and M. F. Ashby, *J. Appl. Phys.* **85**, 7528 (1999).
- ²X. Wang and T. J. Lu, *J. Acoust. Soc. Am.* **106**, 756 (1999).
- ³T. J. Lu, F. Chen, and D. He, *J. Acoust. Soc. Am.* **108**, 1697 (2000).
- ⁴U. Ingard, *J. Acoust. Soc. Am.* **25**, 1037 (1953).
- ⁵D. Maa, *Sci. Sin.* **18**, 55 (1975).
- ⁶D. Y. Maa, *J. Acoust. Soc. Am.* **104**, 2861 (1998).
- ⁷Z. Liu, X. Zhang, Y. Mao, Y. Y. Zhu, Z. Yang, C. T. Chan, and P. Sheng, *Science* **289**, 1734 (2000).
- ⁸J. Li and C. T. Chan, *Phys. Rev. E* **70**, 055602 (2004).
- ⁹N. Fang, D. Xi, J. Xu, M. Ambati, W. Srituravanich, C. Sun, and X. Zhang, *Nat. Mater.* **5**, 452 (2006).
- ¹⁰H. Chen and C. T. Chan, *Appl. Phys. Lett.* **91**, 183518 (2007).
- ¹¹Y. Cheng, F. Yang, J. Y. Xu, and X. J. Liu, *Appl. Phys. Lett.* **92**, 151913 (2008).
- ¹²Z. Yang, J. Mei, M. Yang, N. H. Chan, and P. Sheng, *Phys. Rev. Lett.* **101**, 204301 (2008).
- ¹³G. Ma and P. Sheng, *Sci. Adv.* **2**, e1501595 (2016).
- ¹⁴N. J. R. K. Gerard and Y. Jing, *MRS Commun.* **10**, 32 (2020).
- ¹⁵Y. Li, C. Shen, Y. Xie, J. Li, W. Wang, S. A. Cummer, and Y. Jing, *Phys. Rev. Lett.* **119**, 035501 (2017).
- ¹⁶H. L. Zhang, Y. F. Zhu, B. Liang, J. Yang, J. Yang, and J. C. Cheng, *Sci. Rep.* **7**, 44106 (2017).
- ¹⁷Y. Zhu, J. Hu, X. Fan, J. Yang, B. Liang, X. Zhu, and J. Cheng, *Nat. Commun.* **9**, 1632 (2018).
- ¹⁸N. J. R. K. Gerard, H. Cui, C. Shen, Y. Xie, S. Cummer, X. Zheng, and Y. Jing, *Appl. Phys. Lett.* **114**, 231902 (2019).
- ¹⁹Y. Zhu, N. J. R. K. Gerard, X. Xia, G. C. Stevenson, L. Cao, S. Fan, C. M. Spadaccini, Y. Jing, and B. Assouar, *Adv. Funct. Mater.* **31**, 2101947 (2021).
- ²⁰C. Shen and S. A. Cummer, *Phys. Rev. Appl.* **9**, 054009 (2018).
- ²¹Y. Zhu, A. Merkel, K. Donda, S. Fan, L. Cao, and B. Assouar, *Phys. Rev. B* **103**, 064102 (2021).
- ²²Y. Li and B. M. Assouar, *Appl. Phys. Lett.* **108**, 063502 (2016).
- ²³C. Zhang and X. Hu, *Phys. Rev. Appl.* **6**, 064025 (2016).
- ²⁴C. Chen, Z. Du, G. Hu, and J. Yang, *Appl. Phys. Lett.* **110**, 221903 (2017).
- ²⁵F. Wu, Y. Xiao, D. Yu, H. Zhao, Y. Wang, and J. Wen, *Appl. Phys. Lett.* **114**, 151901 (2019).
- ²⁶X. Liu, M. Duan, M. Liu, F. Xin, and C. Zhang, *J. Appl. Phys.* **129**, 195103 (2021).
- ²⁷Y. Tang, F. Li, F. Xin, and T. J. Lu, *Mater. Design* **134**, 502 (2017).
- ²⁸Y. Tang, S. Ren, H. Meng, F. Xin, L. Huang, T. Chen, C. Zhang, and T. J. Lu, *Sci. Rep.* **7**, 43340 (2017).
- ²⁹Y. Tang, F. Xin, L. Huang, and T. Lu, *Europhys. Lett.* **118**, 44002 (2017).
- ³⁰S. Huang, X. Fang, X. Wang, B. Assouar, Q. Cheng, and Y. Li, *Appl. Phys. Lett.* **113**, 233501 (2018).
- ³¹S. Huang, X. Fang, X. Wang, B. Assouar, Q. Cheng, and Y. Li, *J. Acoust. Soc. Am.* **145**, 254 (2019).
- ³²M. Duan, C. Yu, Z. Xu, F. Xin, and T. J. Lu, *Appl. Phys. Lett.* **117**, 151904 (2020).
- ³³J. Guo, X. Zhang, Y. Fang, and Z. Jiang, *Appl. Phys. Lett.* **117**, 221902 (2020).
- ³⁴M. Duan, C. Yu, F. Xin, and T. J. Lu, *Appl. Phys. Lett.* **118**, 071904 (2021).
- ³⁵Y. Xie, A. Konneker, B.-I. Popa, and S. A. Cummer, *Appl. Phys. Lett.* **103**, 201906 (2013).
- ³⁶N. J. R. K. Gerard, Y. Li, and Y. Jing, *J. Appl. Phys.* **123**, 124905 (2018).
- ³⁷Y. Li, S. Qi, and M. B. Assouar, *New J. Phys.* **18**, 043024 (2016).
- ³⁸X. Zhu, K. Li, P. Zhang, J. Zhu, J. Zhang, C. Tian, and S. Liu, *Nat. Commun.* **7**, 11731 (2016).
- ³⁹Z. Jia, J. Li, C. Shen, Y. Xie, and S. A. Cummer, *J. Appl. Phys.* **123**, 025101 (2018).
- ⁴⁰S. Song, X. Yang, F. Xin, and T. J. Lu, *Phys. Fluids* **30**, 023604 (2018).
- ⁴¹Z. Xu, S. Song, F. Xin, and T. J. Lu, *Phys. Fluids* **31**, 013602 (2019).
- ⁴²S. Song, X. Yang, F. Xin, S. Ren, and T. J. Lu, *J. Phys. D: Appl. Phys.* **50**, 235303 (2017).
- ⁴³Z. Xu, X. Peng, X. Liu, F. Xin, and T. J. Lu, *Europhys. Lett.* **125**, 34004 (2019).
- ⁴⁴Z. Xu, W. He, X. Peng, F. Xin, and T. J. Lu, *J. Acoust. Soc. Am.* **148**, 18 (2020).
- ⁴⁵Z. Xu, W. He, F. Xin, and T. J. Lu, *Phys. Fluids* **32**, 093604 (2020).
- ⁴⁶W. He, M. Liu, X. Peng, F. Xin, and T. J. Lu, *Phys. Fluids* **33**, 063606 (2021).
- ⁴⁷D. L. Johnson, J. Koplik, and R. Dashen, *J. Fluid Mech.* **176**, 379 (1987).
- ⁴⁸S. R. Pride, F. D. Morgan, and A. F. Gangi, *Phys. Rev. B* **47**, 4964 (1993).
- ⁴⁹J. F. Allard and N. Atalla, *Propagation of Sound in Porous Media Modelling Sound Absorbing Materials*, 2nd ed. (John Wiley & Sons Ltd., West Sussex, 2009).
- ⁵⁰Acoustics Module User's Guide, COMSOL Multiphysics version 5.5; <https://doc.comsol.com/5.4/doc/com.comsol.help.aco/AcousticsModuleUsersGuide.pdf>
- ⁵¹Standard Test Method for Impedance and Absorption of Acoustical Materials Using a Tube, Two Microphones and a Digital Frequency Analysis System. ASTM Standards Source, Philadelphia (2019).
- ⁵²User Manual: Impedance Tube Kit Type 4206, Brüel & Kjær.